Carbon 188 (2022) 114–125

Contents lists available at ScienceDirect

Carbon

journal homepage: www.elsevier.com/locate/carbon

Dimensionality effect of conductive carbon fillers in $LiNi_{1/3}Mn_{1/3}Co_{1/3}O_2$ cathode

Cheng-Hung Lin [a], Zhengyu Ju [b], Xiaoyin Zheng [a], Xiao Zhang [b], Nicole Zmich [a], Xiaoyang Liu [a], Kenneth J. Takeuchi [a, c, d], Amy C. Marschilok [a, c, d], Esther S. Takeuchi [a, c, d], Mingyuan Ge [e], Guihua Yu [b, **], Yu-chen Karen Chen-Wiegart [a, e, *]

[a] Department of Materials Science and Chemical Engineering, Stony Brook University, Stony Brook, NY, 11794, USA
[b] Materials Science and Engineering Program, Texas Materials Institute, The University of Texas at Austin, Austin, TX, 78712, USA
[c] Energy and Photon Sciences Directorate, Brookhaven National Laboratory, Upton, NY, 11973, USA
[d] Department of Chemistry, Stony Brook University, Stony Brook, NY, 11794, USA
[e] National Synchrotron Light Source II, Brookhaven National Laboratory, Upton, NY, 11973, USA

ARTICLE INFO

Article history:
Received 14 August 2021
Received in revised form
5 November 2021
Accepted 6 November 2021
Available online 10 November 2021

Keywords:
Lithium-ion battery
Single-walled carbon nanotubes
Morphological degradation
Chemical heterogeneity
Mosaic tomography
XANES tomography

ABSTRACT

Developing advanced electrode architectures through modifying active materials, conductive fillers, binders, and electrolytes as well as processing methods has drawn significant research interest. Due to the insufficient electrical conductivity of many active materials, adding conductive carbon fillers to composite electrodes provides the necessary electrical conductivity. The dimensionality effect among different conductive fillers has a significant impact on electrochemistry, which can be associated with morphological and chemical heterogeneities of electrodes. Here, synchrotron X-ray mosaic nano-tomography and X-ray spectroscopy nanoimaging provided direct three-dimensional (3D) visualization and quantification capabilities to investigate the dimensionality effects of Super P (SP) and single-walled carbon nanotube (SWCNT) fillers on the capacity retention of $LiNi_{1/3}Mn_{1/3}Co_{1/3}O_2$ (NMC111). The results indicate that NMC/SWCNT electrodes, with a wrapping effect from the SWCNTs, exhibited more homogeneous particle size distributions, morphological changes, and chemical states than NMC/SP electrodes, without the wrapping effect. This work developed a framework of 3D quantification methods to study the capacity fading behavior associated with morphological and chemical heterogeneities and paved the way toward designing electrodes for high rate energy storage applications.

1. Introduction

Lithium-ion batteries (LIBs) have been the dominant rechargeable source to power portable electronics in recent years and are regarded as promising candidates for next-generation energy storage for electric vehicles and grids [1–3]. Despite their well-functioning performance in consumer electronics, LIBs with higher energy density and efficiency are required to fulfill the rapid growing demand for next-generation energy storage [1–3]. Therefore, efforts have been devoted to improving the performance of LIBs by modifying different battery components, including active materials, conductive fillers, binders, and electrolytes, as well developing novel processing strategies [3–9]. In addition to creating novel materials, building a thick electrode architecture as an alternative strategy also provides a feasible, straightforward pathway to improve the energy density without significantly altering the fundamental battery chemistry [9–11]. However, the thick electrode design also increases the charge transfer distance for both electrons and ions [11,12]. More convoluted conductive pathways in the thickness direction could lead to more sluggish transport kinetics, poorer rate capability, and lower utilization of active materials in thick electrodes [13–16]. Various approaches, such as building low tortuosity and high porosity structures, have been proposed to improve the ionic diffusion kinetics in thick electrodes [15,17–19]. To enhance electron transport, developing novel conductive carbon fillers and interconnected conductive

* Corresponding author. Department of Materials Science and Chemical Engineering, Stony Brook University, Stony Brook, NY, 11794, USA.
** Corresponding author.
E-mail addresses: ghyu@austin.utexas.edu (G. Yu), Karen.Chen-Wiegart@stonybrook.edu (Y.-c.K. Chen-Wiegart).

https://doi.org/10.1016/j.carbon.2021.11.014
0008-6223/

networks has been demonstrated to be effective [6,20–22].

Replacing the most commonly added filler, carbon black (CB), with carbon nanotubes (CNTs) and graphene has been shown to achieve better electrochemical performance in LIBs due to higher electrical conductivity and better structural stability [6,23,24]. Prior works in the literature also highlighted the modification of CB or CNTs on the improved stability of electrolyte for the high voltage (>4.6 V) applications [25,26]. Recently, Ju et al. reported the dimensionality effects of Super P (SP), single-walled CNTs (SWCNTs), and graphene nanosheets in thick $LiNi_{1/3}Mn_{1/3}Co_{1/3}O_2$ (NMC111) battery electrodes [27]. Their work showed that the 1D SWCNT filler provided not only high electrical conductivity but also a tightly wrapping architecture, leading to superior performance in NMC111 batteries, with key impacts on the rate performances [27]. It is thus of particular importance to understand the effect of the tightly wrapped architecture of SWCNTs upon further cycling with layered cathode materials, such as $LiNi_{1-x-y}Mn_xCo_yO_2$ (NMC). While being one of the most promising insertion-reaction cathode materials for use in LIBs, as-synthesized NMC particles usually have a hierarchical structure with agglomeration of submicron primary particles to form secondary particles that are tens of micrometers in size [28,29]. While recent works used surface treated and single-crystal NMC to improve the performance of the batteries [30,31], most commercially available NMC materials are polycrystalline. During cycling, deagglomeration or fragmentation of secondary particles may coincide with the formation of intergranular cracks and decohesion among primary particles, mainly due to anisotropic volume expansion and contraction [29,32–34]. The development of cracks or fractures associated with secondary particles can lead to capacity fade and is largely influenced by the Ni composition in NMC, current density, and voltage window [35–37]. Therefore, monitoring and characterizing the structural defects, *i.e.*, the cracks and fragments, is crucial to understanding how conductive fillers with different dimensionalities affect the formation of defects and how the wrapping effect of SWCNT filler mitigates cracking or reduces the negative effects of cracks.

The cracks resulting from the degradation of secondary NMC particles are 3D defects that undergo complex chemical and morphological evolution on multiple length scales, from nanoscale to mesoscale, and a 3D analysis method with a range of detection capabilities is required to fully characterize the phenomena [29]. Transmission X-ray microscopy (TXM), available at advanced synchrotron X-ray light sources, is appropriate for this range of scales [38–41]. TXM can provide a field of view on the order of tens of micrometers while achieving relatively high spatial resolution, ~30 nm for hard X-rays [42,43]. With the spatial resolution on the order of tens of nm and the incident X-ray energy that can access the binding energy of the transition metals (6–10 keV), TXM uniquely bridges the gap between the optical microscopy and electron microscopy in terms of the balance between the field of view, spatial resolution and penetration depth. Combined with computed tomography (CT) and quantitative image analysis, the nano-tomography capability in TXM enables correlating the internal 3D nanostructure of the active materials to the cell performance [44–46]. Due to the ability to collect X-ray nanotomography data within 1–2 min at the Full-field X-ray Imaging (FXI) beamline at the National Synchrotron Light Source II (NSLS-II), this work extends the size of the 3D imaging volume to a few hundred micrometers by using a mosaic tomographic mode. Because the contrast mechanism is based on the X-ray attenuation, TXM further enables X-ray absorption near edge structure (XANES) spectroscopic imaging and tomography by tuning incident synchrotron X-ray energies to track 2D and 3D chemical information in electrochemical systems [47,48]. Bulk XAENS spectroscopy provides averaged chemical information such as determining oxidation states and identifying chemical compounds. Through identifying the spectra feature in 3D XANES imaging voxel by voxel computationally, the 3D spatial distribution of the chemical states can be quantified to understand the chemical heterogeneities in complex materials [49–51].

Therefore, using mosaic nanotomography and XANES imaging, this work aims to investigate the role of the dimensionality effects of conductive fillers in retaining the capacity from the aspect of morphological and chemical evolution within NMC111 materials. A notable difference in capacity retention is observed between the cells with NMC/SP and NMC/SWCNT composite electrodes after 200 cycles under a 1C charging/discharging rate. The morphological and chemical evolution, with and without the wrapping effect in the NMC electrode architectures, are discussed based on 3D visualization and quantification. Our results indicate that NMC/SWCNT electrodes with the wrapping effect exhibit more homogeneous spatial distributions of particle size, morphological changes and chemical states than do NMC/SP electrodes without the wrapping effect. Through morphological quantification conducted on a larger, representative volume using mosaic nanotomography while maintaining the needed spatial resolution and spatially resolved chemical mapping by XANES imaging, the framework and methodology developed in this work could also be used to study chemical and morphological changes in a wider range of energy storage materials, thus paving the way toward creating novel electrode designs for high rate capability and long cycle-life batteries.

2. Experimental methods

2.1. Electrode Fabrication, cell assembly, and electrochemical characterization

2.1.1. Electrode fabrication

The NMC/SP electrodes were prepared by mixing NMC111 powder (MTI Corp.), SP (MTI Corp.) and polyvinylidene fluoride (PVDF; Sigma-Aldrich) at a ratio of 90:5:5 in N-methyl-2-pyrrolidone (NMP). After mixing in a Thinky Mixer for 1 h, the viscous slurry was cast on aluminum foil with a doctor blade and further dried in a vacuum oven overnight at 90 °C. The NMC/SWCNT electrodes were prepared by mixing NMC powder, SWCNTs (XFNANO, Inc.) and polyvinylpyrrolidone (PVP, Mw: ~10,000; Sigma-Aldrich) at a ratio of 99:0.5:0.5 in deionized water. PVP served as the surfactant to disperse the SWCNTs in water with probe sonication at 200 W for 2 h. The concentration of SWCNTs in the suspension was 2 mg mL^{-1}. After casting the slurry on ozone-treated aluminum foil, the electrode was first dried in an oven at 60 °C to evaporate water in a mild process and then transferred into a 90 °C vacuum oven to completely remove the residual water. The loading of the as-prepared NMC electrodes was ~15 mg cm^{-2}.

2.1.2. Cell assembly and electrochemical/morphological characterization

CR2032 coin cells were assembled inside an Ar-filled glovebox using a Li plate (Sigma-Aldrich) as the anode. A Celgard 2320 was used as the separator between the NMC cathode and Li anode. 1.0 M $LiPF_6$ dissolved in ethylene carbonate (EC) and diethyl carbonate (DEC) was used as the electrolyte (A6; BASF Corp.). Sixty μL of the electrolyte was used to prepare all coin cells.

Cycling stability measurements were conducted on a Neware battery tester (BTS 4000) with an electrochemical potential window of 2.8–4.25 V *vs.* Li^+/Li. The fresh cell was first activated under a current rate of 0.1C (1C = 150 mA g^{-1}) for 1 cycle and then charged and discharged under 1C for 200 cycles.

2.2. Synchrotron characterization and data analysis

2.2.1. Sample preparation for X-ray nanoimaging

The cycled NMC/SP and NMC/SWCNT cells were disassembled in an Ar-filled glove box within 20 min after the 200th discharged state was reached at 2.8 V to obtain the NMC electrodes. The cycled electrodes were washed with 400 μl 1,2-dimethoxyethane (DME), dried, and resealed into empty coin cells, which were then transferred to the NSLS-II synchrotron facility for characterization. The resealed coin cells were opened in another Ar-filled glove box at NSLS-II, Brookhaven National Laboratory (BNL). Each NMC electrode, including the current collector, was cut into a wedge shape with a tip size less than 50 μm and mounted onto stainless steel pins. To protect the cycled electrodes from being exposed to the air during TXM measurements, each of the cut electrodes was sealed in a Kapton capillary with Torr seal epoxy, stored in the glove box, and transferred to the beamline immediately before the measurements [46]. The TXM samples of pristine NMC electrodes were also prepared with the same cutting and mounting method.

2.2.2. X-ray nanoimaging through transmission X-ray microscopy

X-ray nanoimaging experiments were conducted through transmission X-ray microscopy (TXM) at the Full-field X-ray Imaging beamline (FXI, 18-ID) at NSLS-II of Brookhaven National Laboratory [42]. In this work, the TXM at FXI provided a field of view of 51.2 μm × 43.2 μm (1280 pixels × 1080 pixels) under a camera binning of 2 × 2 with an effective pixel size of 40 nm. The energy of the incident X-ray was above the Ni K-edge (8.333–8.4 keV) to maximize the absorption contrast of Ni in the NMC. To increase the statistical representation for the morphological study, nanotomography based on the absorption contrast was carried out in mosaic tomography mode to significantly extend the imaging volume. The step size to collect the mosaic volume was 30 μm in all three orthogonal directions, x, y and z. The number of acquired mosaic volumetric tiles and the effective volume for each characterized electrode are summarized in Table S1.

For chemical state mapping by spectroscopic imaging, a series of 2D TXM images and 3D tomographic data sets were collected as a function of incident X-ray energy across the Ni K-edge (8.333 keV) to obtain the distributions of the Ni oxidation state in the NMC phase. 2D and 3D XANES images of the post-cycled NMC electrodes were obtained by scanning the Ni K-edge from 8.3 to 8.553 keV with 110 energy points. The 2D XANES imaging was collected from two orthogonal directions, one projecting along the thickness direction of the electrode, providing a “top-down view” into the electrode, and another projecting from the side of the electrode, providing a pseudo “cross-section view” of the cut electrodes to obtain depth-related information.

2.2.3. 3D morphological quantification analysis – particle size and edge gradient

The tomographic data were reconstructed with a Parzen window filter [52] and the filter back projection (FBP) algorithm embedded in the ASTRA plug-in of TomoPy [53]. The full mosaic tomographic data sets were assembled into a complete volume according to the positions of the high-precision piezo stages recorded during the scans under further downsampling with an effective voxel size of 160 nm. Because of the step size (30 μm) used for collecting the mosaic volume, a subvolume of 30 × 30 × 30 μm^3 from each of the reconstructed volumes was used for stitching. The assembled mosaic volumes were then segmented into binary data sets based on the thresholding value between the corresponding peaks in the global histogram of the 3D volume: one value represented the NMC phase, while the other was for the non-NMC domain, including the pores and carbon phases.

To more accurately identify the defects or cracks that may be oversegmented in global thresholding, the watershed algorithm [54] with two geometric criteria to correct the oversegmentation [55,56] was applied. The first criterion was to join the regions where one shared surface connects to more than three different regions. The second criterion was to join the two regions with a critical ratio of the shared surface area and the volume of two adjacent regions [56]. Once each individual particle was identified and labeled, the centroid position of each particle and the straight distance from the centroid to the particle surface (D_{CS}) could be determined by the exact Euclidean distance transform [57]. The average D_{CS} was calculated for each particle. The particle size distribution can then be compared by a certain range of average D_{CS} with the corresponding volume fraction. Meanwhile, the average volume per particle along the direction of electrode thickness was also calculated. A running average was calculated with a 3D window size of 6 μm along the thickness direction (y). The total number of voxels corresponding to NMC within the 3D window was then averaged by the number of labeled particles to obtain the running average volume per particle from the current collector to the surface.

To estimate the distribution of the structural features, such as cracks and fractures, of the NMC particles, the edge gradient was quantified by the smallest eigenvalues of the structure tensor analysis [39,58,59]. The features of the NMC particles were first outlined in the edge detection via the Canny edge detection algorithm [60] based on the watershed segmented data. The edge gradient was then obtained by 3D mean filtering the smallest eigenvalues of the structure tensor based on edge detection using a Python program developed in-house with well-established open-source packages [61,62]. The 2D virtual cross-section images and 3D volumes were visualized with Tomviz (open source) [63] and Dragonfly (noncommercial license) [64] software and the reconstructed data.

2.2.4. XANES imaging analysis

The energy of the XANES images was calibrated with a Ni metal foil and aligned to the Ni K-edge at 8.333 keV. The 2D XANES images were first processed in a PyXAS package developed at the FXI beamline [65], including downsampling with an effective pixel size of 160 nm to improve the signal-to-noise ratio, aligning the images collected at different energies with a StackReg method, and performing the normalization of the XANES spectra for every pixel. The chemical state of each pixel was then determined by Gaussian fitting of the white-line energy position from the spectroscopic image, which corresponds to the energy with maximum X-ray attenuation [48]. Standard XANES spectra for the pristine NMC electrode and the fully charged NMC electrode (at 4.25 V) were measured at the Beamline for Materials Measurement (BMM, 6-BM) at NSLS-II of BNL in the Ni K-edge energy region using transmission geometry. The Athena software package was used to calibrate, merge multiple scans, and perform normalization of the XANES data [66], and the oxidation states of Ni in the standard samples were also confirmed by fitting the white-line energy position with a Gaussian function.

For 3D XANES data processing, all tomographic data were first reconstructed using the same method mentioned previously. After reconstruction, the 110 reconstructed volumes were aligned three-dimensionally through image registration or the 3D StackReg method in PyXAS [65]. Each aligned tomographic data point was then downsampled to an effective pixel size of 160 nm and smoothed by a 2-pixel 3D median filter to improve the signal-to-noise ratio. Once aligned, the 3D XANES data can then be treated as a total of 270 2D XANES image stacks. The chemical state of each voxel was then determined by Gaussian fitting of the white-line

energy position from the reassembled 2D XANES images with the same method used for the 2D XANES image analysis. Once the chemical state of each voxel was obtained, the 3D visualizations of the chemical distribution in postcycled NMC electrodes were rendered by using Tomviz (open source) [63] and Dragonfly (noncommercial license) [64] software.

3. Results and discussions

3.1. Capacity retention difference upon cycling

To equitably compare the electrochemical performance, the content of the conductive fillers was optimized to 5 wt% for SP and 0.5 wt% for SWCNTs to reach the same level of charge-transfer resistance within the composite electrodes [27]. The scanning electron microscopy (SEM) images in Fig. S1 show the different wrapping structures of SWCNTs vs. SP in the pristine NMC electrodes. SWCNTs tightly wrapped NMC particles and formed a better interconnection between NMC particles than the SP. The assembled cells were first activated at a rate of C/10 for 1 cycle and then cycled at a rate of 1C for extended cycling, with a potential window of 2.8 V–4.25 V *vs.* Li^+/Li. The charge/discharge curves of the NMC/SWCNT electrode (0.5 wt%) and NMC/SP electrode (5 wt%) are shown in Fig. S2 at the C-rates of 0.2, 0.5, 1 and 2C. The capacity retention and Coulombic efficiency of the cells with NMC/SPs and NMC/SWCNTs are shown in Fig. 1(a). The capacity of the cells with both conductive fillers decreased as the number of cycles increased. However, a notable capacity retention difference of the cells between the two fillers was found after ~150 cycles, where the capacity of the NMC/SP cell decayed much faster than that of the NMC/SWCNT cell. The SEM images in Fig. 1(b–g) and Fig. S3 show the morphology of the NMC electrodes after 200 cycles with SP and SWCNT additives from the top-down view and cross-section view, respectively. As highlighted with red dashed lines in Fig. 1(c and d), some structural degradation that correlates to the cracks or deagglomeration of the secondary NMC particles was observed. This morphological difference caused by structural degradation may reflect the difference in the capacity retention between the SP and SWCNT conductive fillers upon cycling. The capacity decay resulting from the fragmentation of the secondary particles associated with intergranular cracks or decohesion among primary particles has been reported previously [37–40,67,68]. Below, we present further morphological and chemical quantification by X-ray nanotomography with a greater representative volume. By covering the length scale from that of the NMC particles to that of the electrode, the analysis aims to elucidate the difference in the capacity retention among the cells with SP and SWCNT fillers.

3.2. Representative 3D morphological quantifications with nanoscale spatial resolution

Mosaic nanotomography was applied to the NMC/SP and NMC/SWCNT electrodes in the pristine state and after 200 cycles, when cells were in the discharged state (2.8 V *vs.* Li^+/Li). The 3D volume rendering of the stitched mosaic tomography consisting of thousands of NMC particles is shown in Fig. 2 and the supporting information (Video S1-Video S4). Although the volume rendering provided a direct visualization of the electrodes, to compare the morphological evolution, quantitative analysis based on the 3D images was needed. To quantify the morphological evolution upon cycling, the particle size distribution and the average volume of particles in the NMC electrodes are shown in Fig. 3. Fig. 3(a) illustrates an example of the distance map of NMC particles where the position of the centroid and the distance from the centroid to the particle surface, D_{CS}, are color coded. Notably, the particle surface has a value of unity (voxel) in the distance map. The D_{CS} values for each particle were averaged to obtain a representative feature size (average D_{CS}), as shown in Fig. S4 and Fig. 3(b and c). The particle size distribution of the NMC characterized by the volume fraction *vs.* the average D_{CS} is shown in Fig. S4(a), with the derived cumulative version shown in Fig. S4(b) and Fig. 3(b and c). Fig. 3(d) shows the average volume per particle along the direction of electrode depth from the current collector to the electrode surface as a running average in every slice along the depth direction with a 6-μm thick moving window. In Fig. 3(c), the NMC/SWCNT electrodes show an overall size distribution that shifted toward a smaller particle size after 200 cycles. The size distribution in Fig. 3(d) also indicates that NMC/SWCNT electrodes had a more uniform size distribution along the electrode direction, and that the size of particles decreased after 200 cycles. This homogeneously decreasing particle size after cycling in NMC/SWCNTs can be related to some structural degradation, leading to the slight capacity decay in Fig. 1(a). In contrast, the depth-dependent size distribution in the NMC/SP electrodes showed a greater variation and thus, overall less homogeneous structure. Similarly, the size distribution in the NMC/SP pristine sample had an overall larger fluctuation than the NMC/SP after 200 cycles, as shown in Fig. 3(b). When the average D_{CS} was smaller than ~5 μm, pristine NMC/SP had a larger cumulative volume fraction. In contrast, pristine NMC/SP exhibited a smaller cumulative volume fraction when the

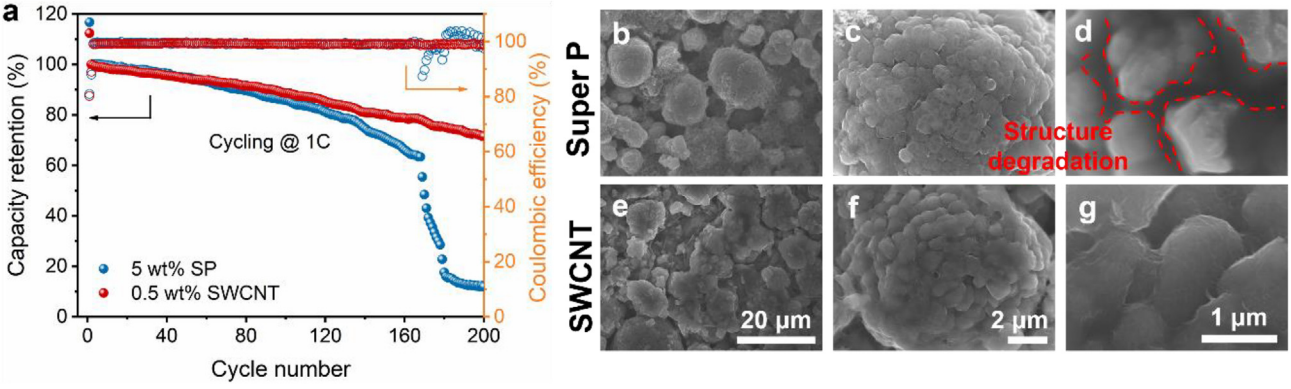

Fig. 1. The cycling behaviors of the NMC cells with two different conductive fillers and the SEM images of the postcycled NMC electrodes. (a) The capacity retention and Coulombic efficiency of the NMC/SP (blue) and NMC/SWCNT (red) cells. (b–g) Top-down view SEM images of the cells with (b–d) NMC/SP and (e–g) NMC/SWCNTs after 200 cycles. (A colour version of this figure can be viewed online.)

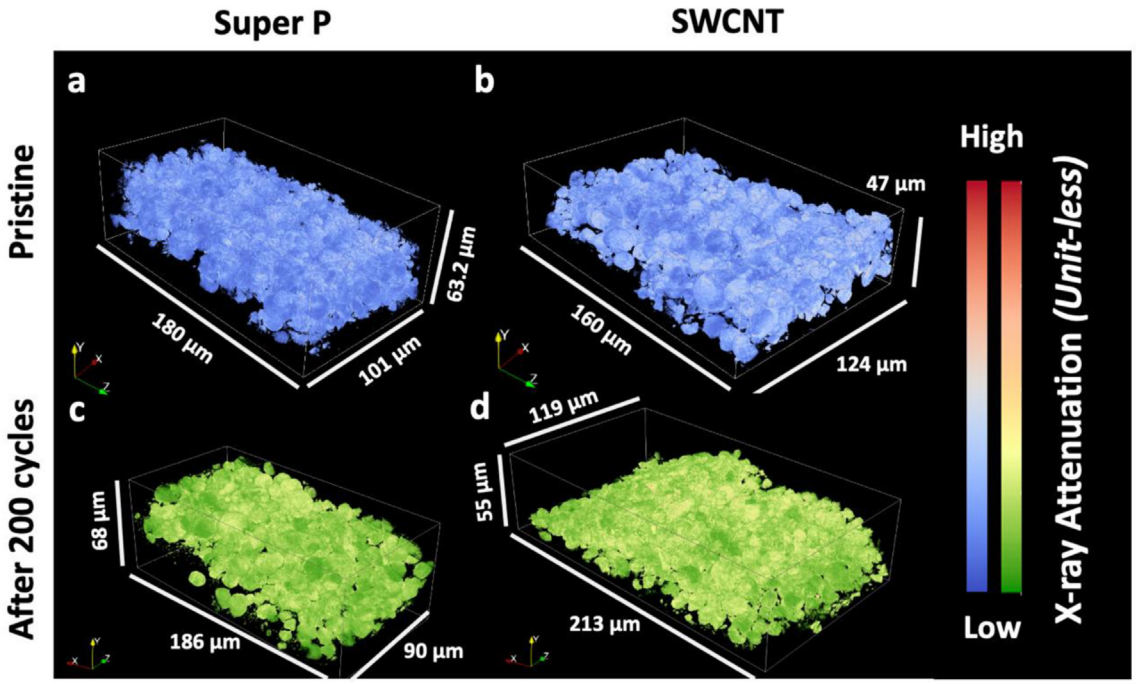

Fig. 2. The stitched volume of the mosaic tomographic data based on the X-ray absorption contrast. (a) NMC/SP in the pristine state; (b) NMC/SWCNTs in the pristine state; (c) NMC/SP after 200 cycles; (d) NMC/SWCNTs after 200 cycles. Animations of each stitched volume can be found in the supporting information. (A colour version of this figure can be viewed online.)

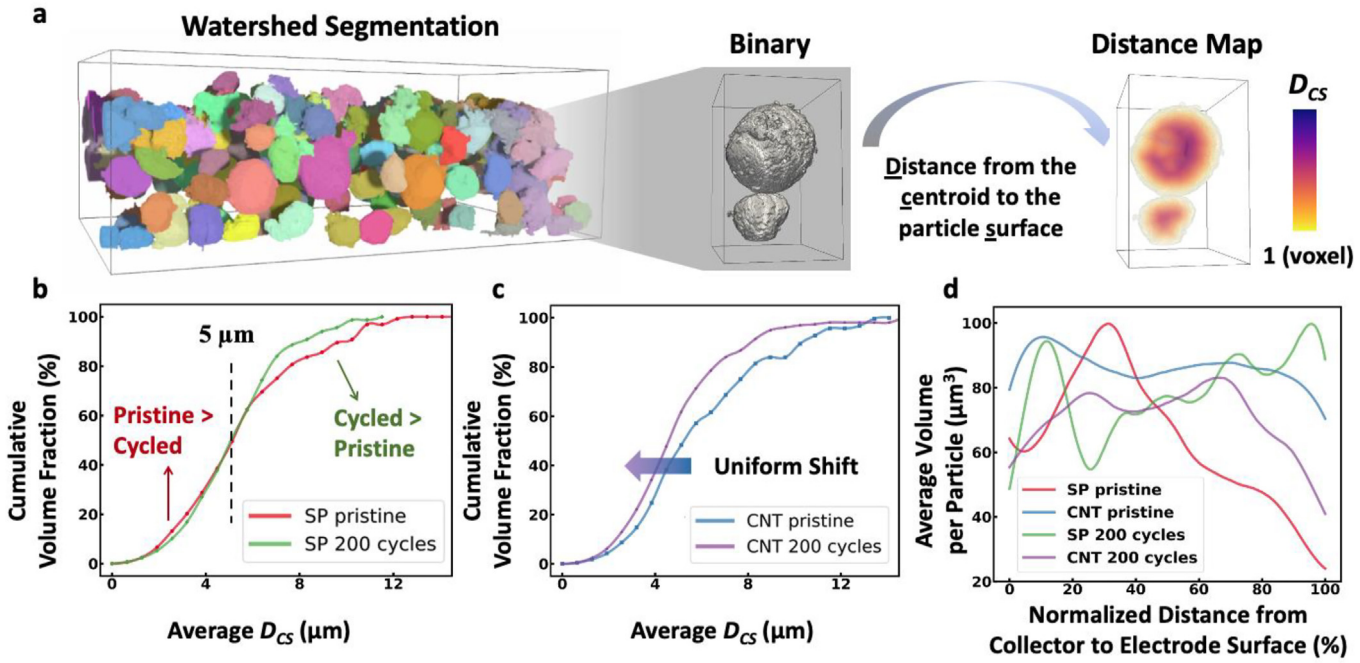

Fig. 3. The particle size distribution of the NMC particles in the electrodes. (a) Schematic of the distance from the centroid to the surface (D_{CS}) derived from the map of the Euclidean distance transform. (b, c) Particle size distributions of NMC/SP (b) and NMC/SWCNT electrodes (c) in the pristine and 200-cycle states, characterized by the average D_{CS} and the cumulative volume fraction. (d) The average volume per particle along the electrode thickness direction from the current collector to the free surface with a step size of 6 µm. (A colour version of this figure can be viewed online.)

average D_{CS} > 5 µm. Further analysis regarding this observation is discussed in the following sections.

Supplementary data related to this article can be found at https://doi.org/10.1016/j.carbon.2021.11.014.

Supplementary video related to this article can be found at https://doi.org/10.1016/j.carbon.2021.11.014

To further quantify the morphological evolution in the NMC electrodes, the features of the NMC particles were characterized in the form of the edge gradient distribution through structure tensor analysis [39,58,59]. By extracting the smallest eigenvalues in the structure tensor calculation, the fracturing features of the NMC electrodes, such as fragments and cracks, are visualized by a color

scale in Fig. 4, Fig. 5, and Fig. S5 to evaluate the local degree of morphological changes [39,40,69]. A larger value of the edge gradient reflects a higher degree of morphological change in the NMC particles, in which the local structural change mainly results from crack formation. Fig. 4 shows the evolution of the morphological degradation in the NMC/SWCNT electrodes before and after 200 cycles. In the pristine state, the NMC/SWCNT electrode has a homogeneous distribution of the edge gradient along the thickness direction, as shown in the virtual slides near the surface *vs.* near the current collector (Fig. 4(b and c)) and the histograms in Fig. 4(g and h). This observation is consistent with the uniform size distribution of the NMC/SWCNT pristine electrode shown in Fig. 3(d). However, the NMC/SWCNT electrode, after 200 cycles, demonstrated a steeper distribution of the edge gradient in both the visualizations (Fig. 4(d–f)) and the histograms (Fig. 4(g and h)) than the pristine NMC/SWCNT electrode. A steeper edge gradient distribution reflects more morphological degradation. In particular, the region near the surface/separator had even more degradation than the region near the current collector in the NMC/SWCNT electrode after 200 cycles. This indicates that the degradation may have been depth-dependent in the NMC/SWCNT electrodes. The overall steeper edge gradient distribution in the SWCNT 200-cycle state than in the pristine state in Fig. 4 and Figs. S7(a and c) is consistent with the decreasing particle size distribution shown in Fig. 3(c and d). Both the steeper edge gradient distribution and the decreasing size distribution can then explain the morphological degradation leading to the capacity decay of the NMC/SWCNT cell in Fig. 1(a).

However, the distributions of the edge gradient in the NMC/SP electrodes in Fig. S5 show that the NMC/SP pristine electrode had more fragmented features than the NMC/SP electrode after 200 cycles. Especially in Fig. S5(b), the region near the surface of the NMC/SP pristine electrode had the most concentrated fragmented structures in the NMC/SP electrodes. The finding in the analysis of the edge gradient is consistent with the particle size distribution in Fig. 3(b and d), showing that the NMC/SP pristine electrode had an overall smaller but more heterogeneous particle size distribution. The nonuniform particle size distribution in the NMC/SP pristine electrode may be attributed to the electrode manufacturing process. Previous reports have indicated that some morphological heterogeneities, such as a density or a particle size gradient along the thickness direction, could be generated during slurry casting and solvent drying with carbon black and PVDF binder in NMP solvent [70–73]. The use of a planetary mixer while preparing the NMC/SP slurry can provide a better dispersion of the particle clusters but may lead to a higher degree of the deagglomeration of secondary particles that contributes to a smaller particle size distribution [8,74]. These factors increase the morphological inhomogeneity in the NMC/SP electrodes. The smaller particles in the pristine NMC/SP provide a higher initial capacity and maintain a capacity retention similar to that of the NMC/SWCNT cells in early cycling. Nevertheless, the damage from the secondary particles in the NMC/SP electrodes may lead to faster capacity retention decay upon further cycling [29,67,68]. Further analysis focusing on the secondary particles is discussed in the following sections.

To reasonably compare the structural evolution of the NMC/SP 200-cycle electrode observed in Fig. 1(c and d) with the pristine

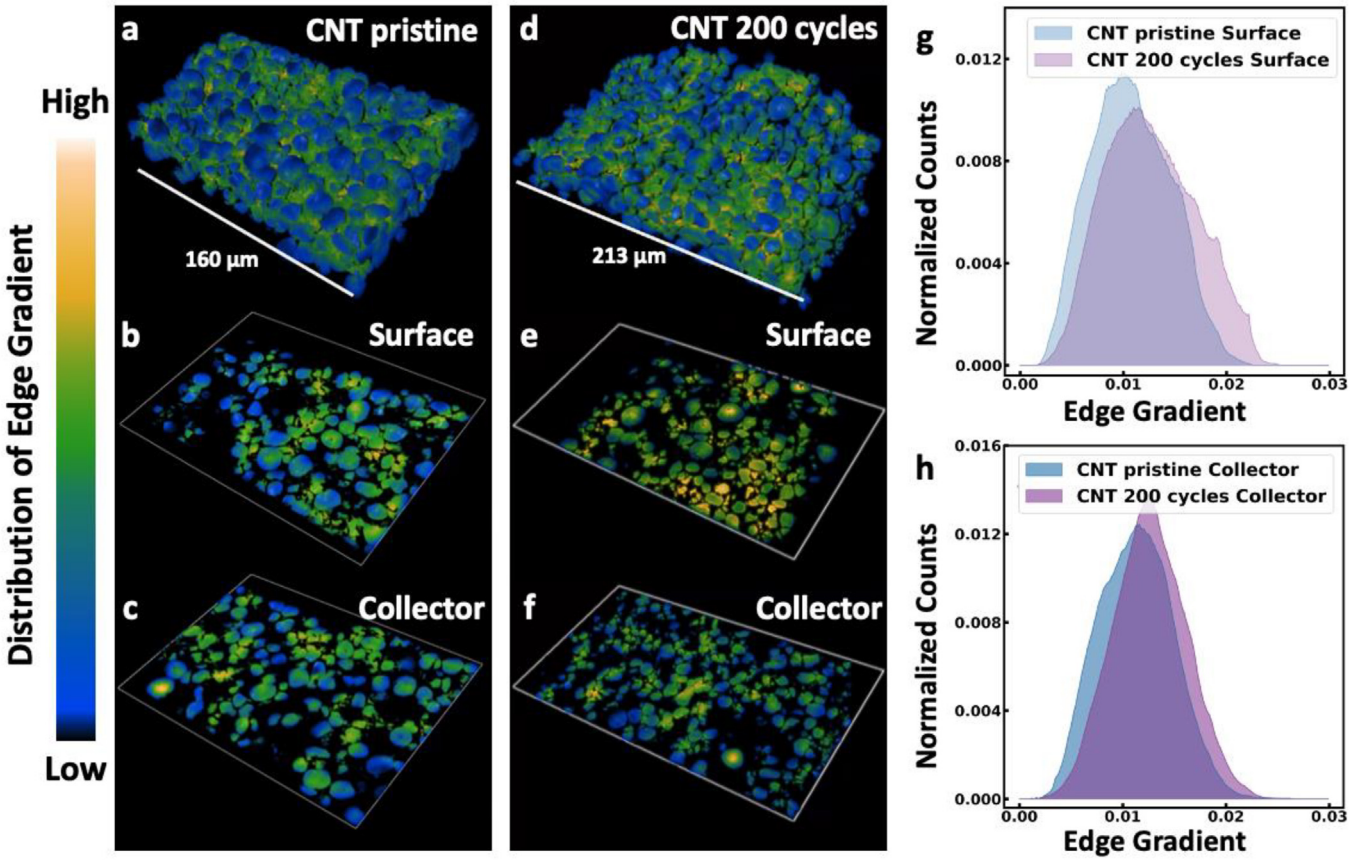

Fig. 4. The distributions of the edge gradients of the NMC/SWCNT electrodes without filtering out particles. (a, d) The 3D profiles of the edge gradients in the NMC/SWCNT electrode, pristine and after 200 cycles, respectively. (b, c, e, f) The lateral slices near the surface/separator vs. near the current collector in (a) and (d). (g, h) The histograms used to compare the edge gradients within a 10-µm thick volume near the surface/separator (g) and near the current collector (h) in the pristine and post-cycled states. (A colour version of this figure can be viewed online.)

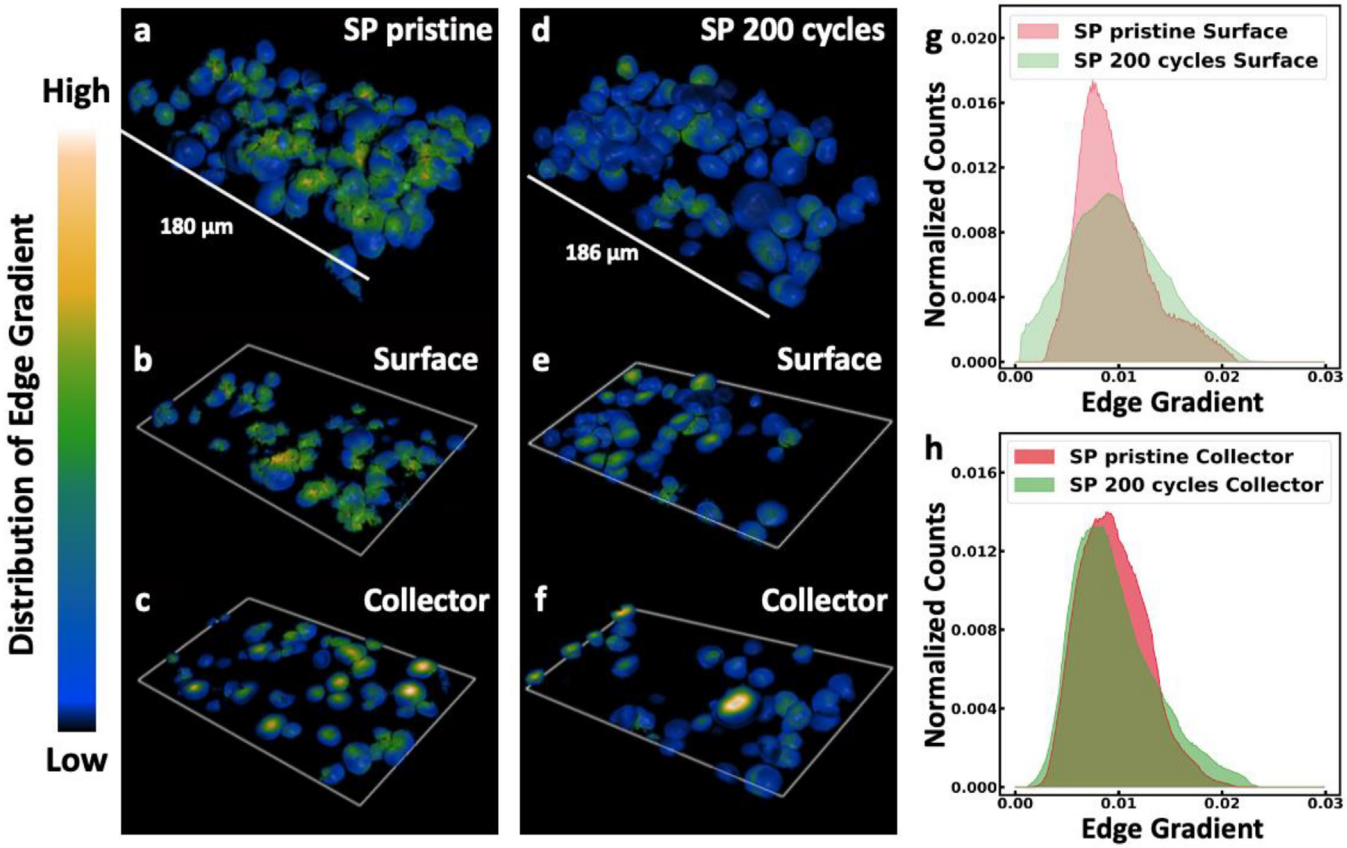

Fig. 5. The distributions of the edge gradients of the NMC/SP electrodes after filtering out the particles with effective radius smaller than 5 μm. (a, d) The 3D profiles of the edge gradient in the NMC/SP electrode, pristine and after 200 cycles, respectively. (b, c, e, f) The lateral slices near the surface/separator *vs.* near the current collector in (a) and (d). (g, h) The histograms used to compare the edge gradients within a 10-μm thick volume near the surface/separator (g) and near the current collector (h) in the pristine and post-cycled states. (A colour version of this figure can be viewed online.)

state, the small, fragmented particles in the NMC/SP electrodes, present in the pristine samples, were filtered out, and the morphological analysis focused on the secondary particles. The histogram of the effective spherical radius in Fig. S6 shows a quasi-median distribution at 5 μm of NMC particles in the NMC/SP pristine electrode. Thus, the particles with an effective spherical radius less than 5 μm were masked. Only the particles with radii larger than 5 μm were analyzed in Fig. 5 to characterize mainly the edge gradient distribution from the secondary particles in the NMC/SP electrodes. By filtering the particles, the profiles of the edge gradient distribution in Fig. 5(a–f) were more representative of the secondary particles. However, the histograms of the NMC/SP electrodes (with filtering of the particles) in Fig. S7(d) still showed that the 200-cycle state had a smaller and wider edge gradient distribution. This is probably because part of the morphological degradation in the NMC/SP 200-cycle electrode, such as the fractures of the secondary particles, has also been filtered out. Nevertheless, the histograms in Fig. 5(g and h) show that the NMC/SP 200-cycle electrode had a larger edge gradient distribution at both regions, near the surface/separator and near the current collector, than the pristine state. The region near the surface/separator in the NMC/SP 200-cycle electrode also demonstrates a wider distribution than the region near the current collector. This depth-dependent phenomenon is similar to the result for the NMC/SWCNT 200-cycle electrode shown in Fig. 4(g and h). The regions near the surfaces of both the NMC/SWCNT and NMC/SP 200-cycle electrodes experienced more morphological degradation than the regions near the current collector. The morphological heterogeneity indicated that the degradation of the activated materials occurred inhomogeneously upon the cycling reaction and can be one of the factors leading to capacity decay. In addition to the morphological analysis, further chemical analysis presented in the next section, will provide additional insights to understand the different extents of capacity retention in both types of electrodes.

3.3. Chemical mapping from the view of the electrodes and individual particles

In addition to quantifying the morphological evolution upon cycling, it is also critical to reveal the distribution of chemical states to further understand the capacity retention difference between NMC/SP and NMC/SWCNT cells. In this work, the redox reaction of nickel (Ni^{2+}/Ni^{4+}) contributes to the majority of the delivered capacity [27,75,76]. XANES spectroscopic imaging was employed to map the Ni, Co, and Mn oxidation states but focused on Ni states from multiple views of the NMC/SP and NMC/SWCNT electrodes after 200 cycles. The cells were stopped in the discharged state (2.8 V), *i.e.,* the fully lithiated state. The Ni oxidation states of pristine (Ni^{2+}) and delithiated (Ni^{4+}) NMC were determined by Gaussian fitting of the white-line energy position, as shown in Fig. S8. The standard XANES spectra of Ni, Co, and Mn in Fig. S8 and Fig. S9 were acquired from the bulk XANES measurements to obtain an average of the chemical state in the electrodes. 2D XANES imaging in Fig. 6 projects the Ni oxidation states from the cross-section view and top-down view of the electrodes. 2D XANES imaging in Fig. S10 shows the Co and Mn oxidation states from with

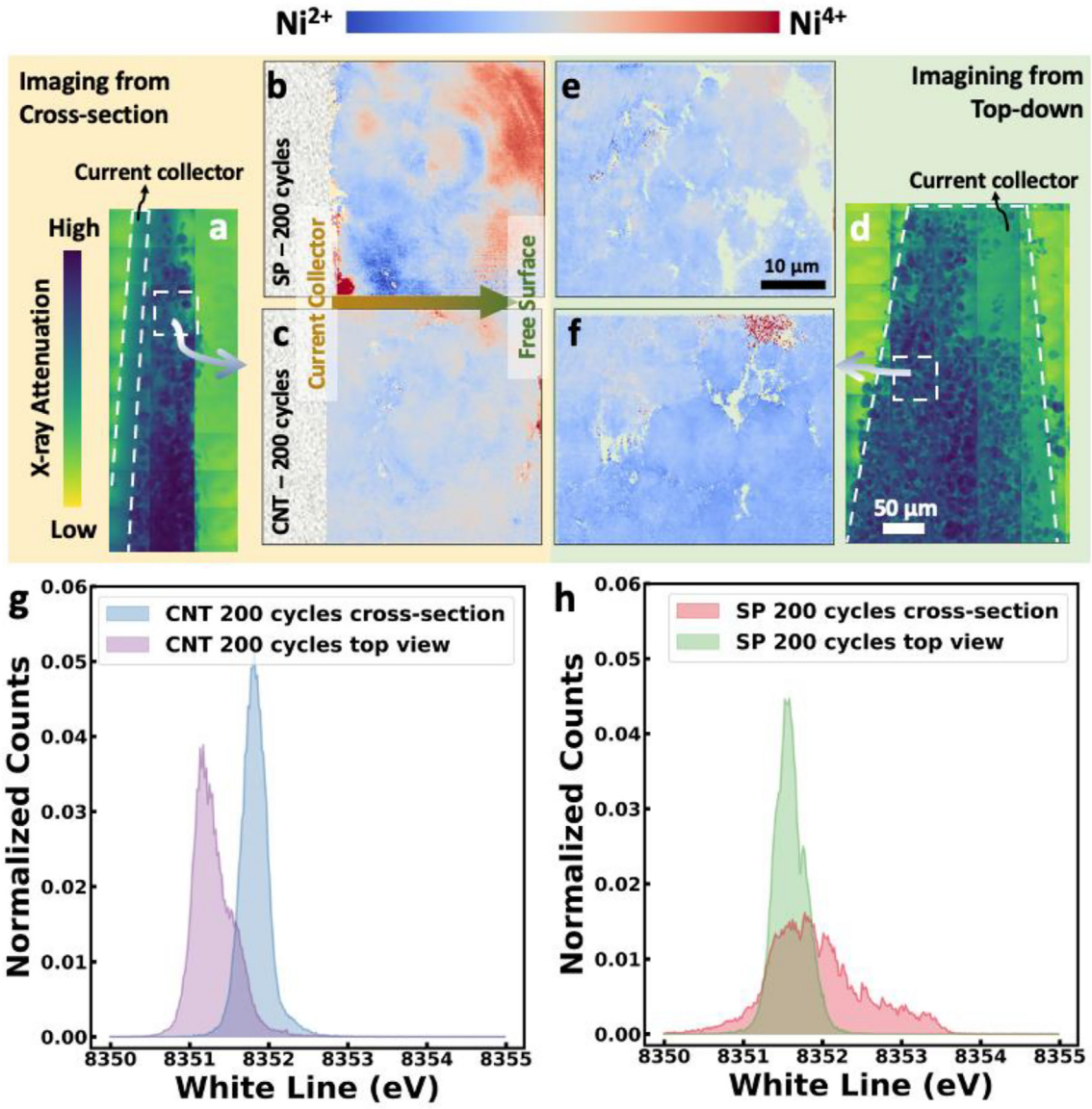

Fig. 6. 2D XANES spectroscopic mapping of Ni oxidation states in the post-cycled NMC electrodes. (a, b, c) Images of the cross-section view of the electrode; (d, e, f) Images of the top-down view of the electrode; (g, h) the histograms of Ni states from the cross-section vs. top-down views of the NMC/SWCNT electrode in (c, f) and the NMC/SP electrodes in (b, e). (a, d) 2D mosaic images of the absorption contrast used to locate the orthogonal projections of the cross-section view (a) and the top-down view (d). (b, e) the NMC/SP and (c, f) NMC/SWCNT electrodes after 200 cycles. In the cross-section view (b, c), the direction from the current collector to the free surface of the electrode is labeled. (A colour version of this figure can be viewed online.)

the same sample position as in Fig. 6(b and c). 3D XANES tomography in Fig. 7 provides the Ni oxidation states within the secondary NMC particles.

In 2D XANES mapping, the NMC/SWCNT electrodes after 200 cycles (Fig. 6(c, f, g) had overall better reaction reversibility and chemical homogeneity from both the cross-section and top views than the NMC/SP electrodes after 200 cycles (Fig. 6(b, e, h)). Especially in the cross-section view, although both the active materials in NMC/SP and NMC/SWCNT electrodes were not completely lithiated, the cross-section chemical mappings in Fig. 6(b and c) and histograms in Fig. 6(g and h) of NMC/SP and NMC/SWCNT electrodes, after 200 cycles, showed different reaction homogeneities. Despite incomplete lithiation, the electrochemical reactions in the NMC/SWCNT electrodes were more homogeneous along the electrode thickness. However, the NMC/SP electrodes, after 200 cycles, in addition to exhibiting even less complete lithiation, showed depth-dependent chemical heterogeneity where fewer reactions occurred in the region near the surface/separator than the region near the current collector. The Ni oxidation state in the NMC111 samples should be 2+ and 4+ in the pristine or completely lithiated and the delithiated states, respectively [75,76]. For Co and Mn, the mapping and histograms in Fig. S10 show homogeneous distributions which are closed to the lithiated/pristine state. This observation strengthens the conclusion that the chemical heterogeneity upon extended cycling results from the incomplete reaction of Ni in NMC and is consistent with the literature where the redox reaction of Ni contributes to the majority of the capacity in NMC cells under the selected voltage range. In addition to the chemical heterogeneity at the electrode level, the distributions of the Ni oxidation states at the level of secondary particles are illustrated as 3D XANES images in Fig. 7. Fig. 7 maps the distributions of the Ni oxidation states, both interparticle and intraparticle, at a region near the

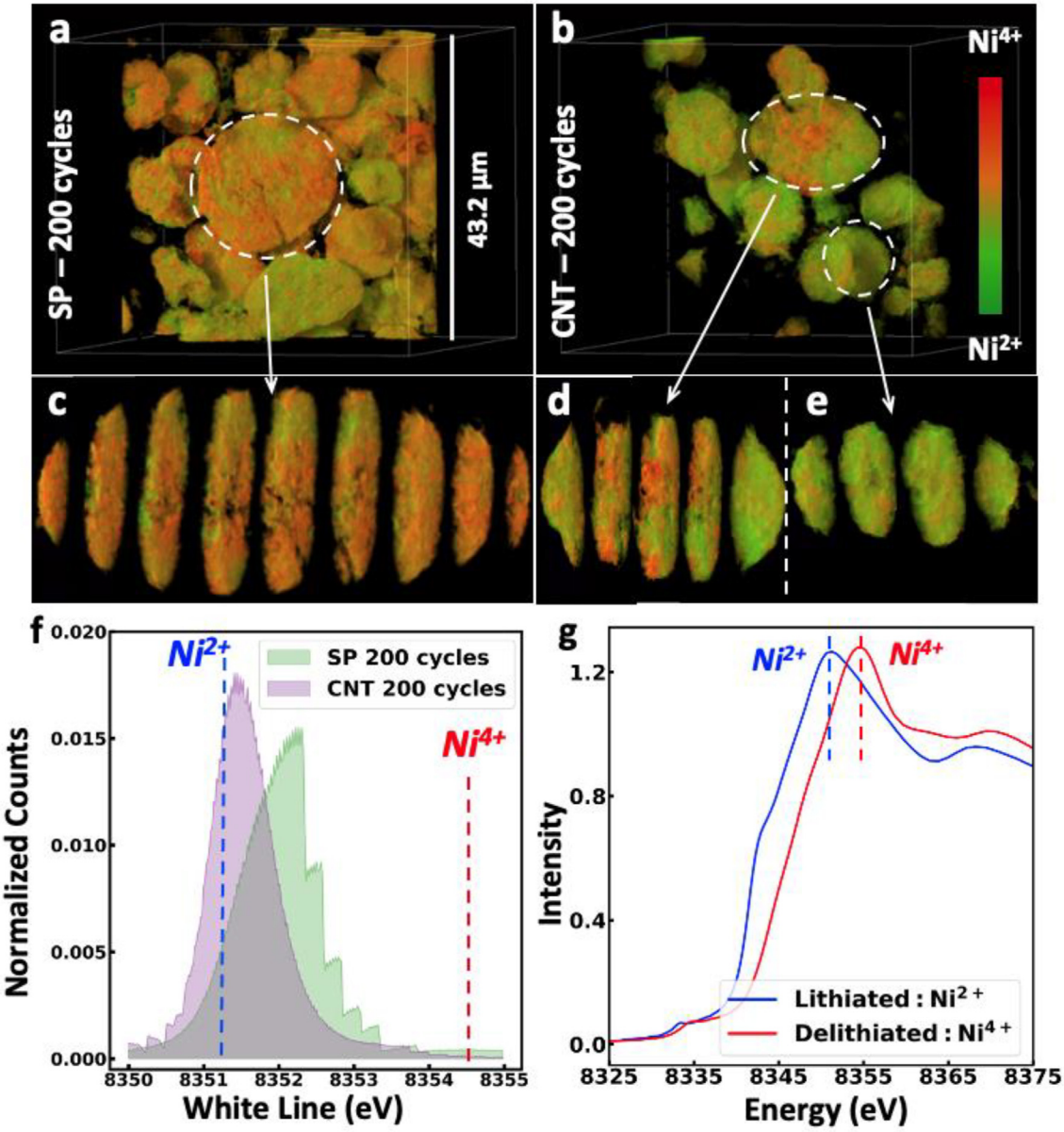

Fig. 7. 3D XANES tomographic mapping of Ni oxidation states in the post-cycled NMC electrodes. (a, c) the NMC/SP and (b, d, e) NMC/SWCNT electrodes after 200 cycles; (f) histograms of 3D XANES in (a) and (b); (g) the standard Ni XANES spectra of lithiated NMC (Ni^{2+}) and delithiated NMC (Ni^{4+}) electrodes. The internal distribution of Ni oxidation states within the particles of the NMC/SP and NMC/SWCNT electrodes are illustrated in (c) and (d, e), respectively. (A colour version of this figure can be viewed online.)

current collector. The mapping of the NMC/SP 200-cycle electrode in Fig. 7(a, c) shows less complete lithiation than the NMC/SWCNT 200-cycle electrode in Fig. 7(b-e). The less complete reaction, which contributed to the higher chemical heterogeneity in the NMC/SP 200-cycle electrode, suggests that the conductive network in the NMC/SP electrode was less efficient than that in the NMC/SWCNT electrode.

The incomplete reaction and the chemical heterogeneity in the 200-cycle electrodes agree with the results of the morphological analysis discussed previously. In the pristine state, the NMC/SWCNT electrode had uniform particle size and edge gradient distributions, while both distributions in the NMC/SP electrode were heterogeneous. The dimensionality effect of the tightly wrapping architecture with the SWCNT filler and the more homogeneous electrode manufacturing process provided a more uniform morphological distribution in the NMC/SWCNT electrode [27,72,73]. After 200 cycles, the lower electronic conductivity of the SP and the lower SP/PVDF interconnectivity, due to the nonuniform particle size distribution in the NMC/SP electrode, resulted in a faster decay of the capacity retention than that of the NMC/SWCNT electrode [27,73,77]. Furthermore, the stronger depth-dependent morphological and chemical phenomena imply that the charging/discharging reaction in the NMC/SP cell was more heterogeneous than that in the NMC/SWCNT cell. The NMC/SWCNT 200-cycle electrode had some morphological degradation, as shown in Fig. 4, but still maintained relatively good chemical homogeneity, as shown in Fig. 6(c). In contrast, the NMC/SP cell exhibited a higher depth-dependent morphological degradation (Fig. 5) and incomplete reaction (Fig. 6(b)); these results agreed with the faster capacity decay of the NMC/SP cell in Fig. 1(a). Previous finite element modeling has indicated the presence of an inhomogeneous electrochemical driving force in which the NMC particles near the

surface/separator experienced higher electron and Li outfluxes at the interface of the particles and the electrolyte [40]. As a result of this nonuniform driving force, the NMC particles near the surface/separator experienced larger diffusion-induced stresses, which then induced more crack formation in those regions than near the current collector [40]. This modeling successfully explains the depth-dependent behaviors shown in Figs. 5 and 6(b) and the capacity fading observed in our NMC/SP electrodes. However, the tightly wrapping architecture and the better electrical conductivity of the SWCNTs mitigated the effect of the inhomogeneous electrochemical driving force [27]. Thus, the NMC/SWCNT 200-cycle electrode showed a lower extent of morphological degradation (Fig. 4) and maintained a more uniform chemical distribution (Fig. 6(c)).

4. Conclusions

In summary, the decay of the capacity retention in thick NMC electrodes with SP and SWCNT conductive fillers is further investigated through measurements of cyclability, morphology, and chemistry. A capacity retention difference (>10%) among the NMC-SP and NMC-SWCNT cells is observed after ~150 cycles, and this difference continues to increase upon further cycling at a 1C rate (>50% after 200 cycles). From SEM, some morphological degradations, such as cracks and isolated primary NMC particles, are found in the NMC/SP 200-cycle electrode, while the architecture of the NMC/SWCNT 200-cycle electrode is well preserved because of the wrapping effect of the SWCNTs.

The morphological analysis in the mosaic tomography mode shows that the NMC/SWCNT electrodes have a uniform particle size distribution in both the pristine and 200-cycle states, but the average particle size decreases after cycling. The homogenously decreased size distribution, increased edge gradient distribution, and chemical state distribution in the NMC/SWCNT 200-cycle electrodes reflect part of the morphological degradation and correspond to the better capacity retention in the NMC/SWCNT cells. In contrast, the particle size distribution in the NMC/SP electrodes is not uniform and can be affected by the manufacturing process. The strong depth-dependent behaviors of the morphological degradation and the chemical heterogeneity in the NMC/SP electrodes are consistent with their faster capacity decay than that in the NMC/SWCNT cells. From 3D XANES, the chemical states of the NMC particles near the current collector with the SP filler are more heterogeneous than those with the SWCNT filler. Compared to the NMC/SP electrodes, the tightly wrapping architecture and the high electrical conductivity of the SWCNT filler demonstrate homogeneous but light morphological degradation, uniform chemical distribution, and better capacity retention upon cycling.

This work provides further understanding of the cycling capability among SP and SWCNT fillers in NMC materials through a multiscale morphological and chemical analyses from the particle to the electrode level. This work also provides a framework to conduct 3D morphological analysis at a nanometer scale with better statistical representation and facilitate the design of advanced electrodes for high-rate applications.

CRediT authorship contribution statement

Cheng-Hung Lin: Conceptualization, Methodology, Formal analysis, Investigation, Data curation, Writing – original draft, Writing – review & editing, Visualization. **Zhengyu Ju:** Conceptualization, Formal analysis, Investigation, Resources, Data curation, Writing – review & editing. **Xiaoyin Zheng:** Data curation, Formal analysis, Investigation. **Xiao Zhang:** Investigation, Resources. **Nicole Zmich:** Formal analysis, Investigation, Writing – review & editing. **Xiaoyang Liu:** Formal analysis, Investigation. **Kenneth J. Takeuchi:** Supervision, Funding acquisition. **Amy C. Marschilok:** Conceptualization, Writing – review & editing, Supervision, Funding acquisition. **Esther S. Takeuchi:** Conceptualization, Writing – review & editing, Supervision, Funding acquisition. **Mingyuan Ge:** Investigation, Writing – review & editing, Supervision. **Guihua Yu:** Conceptualization, Resources, Writing – review & editing, Supervision, Project administration. **Yu-chen Karen Chen-Wiegart:** Conceptualization, Methodology, Formal analysis, Investigation, Writing – review & editing, Supervision, Project administration.

Declaration of competing interest

The authors declare that they have no known competing financial interests or personal relationships that could have appeared to influence the work reported in this paper.

Acknowledgments

This research was supported by the Center for Mesoscale Transport Properties, an Energy Frontier Research Center supported by the U.S. Department of Energy, Office of Science, Basic Energy Sciences, under award #DE-SC0012673. This research used resources and the Full Field X-ray Imaging (FXI) beamline (18-ID) and Beamline for Materials Measurement (BMM) (6-BM) of the National Synchrotron Light Source II, a U.S. Department of Energy (DOE) Office of Science User Facility operated for the DOE Office of Science by Brookhaven National Laboratory under Contract No. DE-SC0012704. The authors are grateful to Dr. Bruce Ravel (National Institute of Standards and Technology), scientist at BMM beamline, for his expertise and support of the BMM experiments. We acknowledge the support of sample preparation, data collection and preliminary analysis during the FXI beamtime provided by the Chen-Wiegart group members. E.S.T. acknowledges the William and Jane Knapp Chair in Energy and the Environment.

Appendix A. Supplementary data

Supplementary data to this article can be found online at https://doi.org/10.1016/j.carbon.2021.11.014.

References

[1] J.B. Goodenough, Electrochemical energy storage in a sustainable modern society, Energy Environ. Sci. 7 (1) (2014) 14–18.
[2] A. Manthiram, An outlook on lithium ion battery technology, ACS Cent. Sci. 3 (10) (2017) 1063–1069.
[3] M. Li, J. Lu, Z. Chen, K. Amine, 30 Years of lithium-ion batteries, Adv. Mater. 30 (33) (2018), 1800561.
[4] K. Xu, Nonaqueous liquid electrolytes for lithium-based rechargeable batteries, Chem. Rev. 104 (10) (2004) 4303–4417.
[5] H. Zhang, H. Zhao, M.A. Khan, W. Zou, J. Xu, L. Zhang, J. Zhang, Recent progress in advanced electrode materials, separators and electrolytes for lithium batteries, J. Mater. Chem. 6 (42) (2018) 20564–20620.
[6] R. Fang, K. Chen, L. Yin, Z. Sun, F. Li, H.-M. Cheng, The regulating role of carbon nanotubes and graphene in lithium-ion and lithium–sulfur batteries, Adv. Mater. 31 (9) (2019), 1800863.
[7] J.L. Liu, C.H. Xu, Z. Chen, S.B. Ni, Z.X. Shen, Progress in aqueous rechargeable batteries, Green Energy Environ 3 (1) (2018) 20–41.
[8] A. Kraytsberg, Y. Ein-Eli, Conveying advanced Li-ion battery materials into practice the impact of electrode slurry preparation skills, Advanced Energy Materials 6 (21) (2016), 1600655.
[9] X. Zhang, Z.Y. Ju, Y. Zhu, K.J. Takeuchi, E.S. Takeuchi, A.C. Marschilok, G.H. Yu, Multiscale understanding and architecture design of high energy/power lithium-ion battery electrodes, Advanced Energy Materials 11 (2) (2021) 20.
[10] H.M. Cheng, F. Li, ENERGY STORAGE Charge delivery goes the distance, Science 356 (6338) (2017) 582–583.
[11] Y.D. Kuang, C.J. Chen, D. Kirsch, L.B. Hu, Thick electrode batteries: principles, opportunities, and challenges, Adv. Energy Mater. 9 (33) (2019) 19.
[12] H.-M. Cheng, F. Li, Charge delivery goes the distance, Science 356 (6338)

(2017) 582–583.
[13] Z.J. Du, D. Wood, C. Daniel, S. Kalnaus, J.L. Li, Understanding limiting factors in thick electrode performance as applied to high energy density Li-ion batteries, J. Appl. Electrochem. 47 (3) (2017) 405–415.
[14] H. Gao, Q. Wu, Y.X. Hu, J.P. Zheng, K. Amine, Z.H. Chen, Revealing the rate-limiting Li-ion diffusion pathway in ultrathick electrodes for Li-ion batteries, J. Phys. Chem. Lett. 9 (17) (2018) 5100–5104.
[15] J.T. Hu, B.B. Wu, X. Cao, Y.J. Bi, S.J. Chae, C.J. Niu, B.W. Xiao, J.H. Tao, J.G. Zhang, J. Xiao, Evolution of the rate-limiting step: from thin film to thick Ni-rich cathodes, J. Power Sources 454 (2020) 7.
[16] Z.Y. Ju, Y. Zhu, X. Zhang, D.M. Lutz, Z.W. Fang, K.J. Takeuchi, E.S. Takeuchi, A. Marschilok, G.H. Yu, Understanding thickness-dependent transport kinetics in nanosheet-based battery electrodes, Chem. Mater. 32 (4) (2020) 1684–1692.
[17] J.S. Sander, R.M. Erb, L. Li, A. Gurijala, Y.M. Chiang, High-performance battery electrodes via magnetic templating, Nat. Energy 1 (8) (2016) 16099.
[18] Y. Zhang, O.I. Malyi, Y. Tang, J. Wei, Z. Zhu, H. Xia, W. Li, J. Guo, X. Zhou, Z. Chen, C. Persson, X. Chen, Reducing the charge carrier transport barrier in functionally layer-graded electrodes, Angew. Chem. Int. Ed. 56 (47) (2017) 14847–14852.
[19] X. Zhang, Z. Ju, L.M. Housel, L. Wang, Y. Zhu, G. Singh, N. Sadique, K.J. Takeuchi, E.S. Takeuchi, A.C. Marschilok, G. Yu, Promoting transport kinetics in Li-ion battery with aligned porous electrode architectures, Nano Lett. 19 (11) (2019) 8255–8261.
[20] R. Raccichini, A. Varzi, S. Passerini, B. Scrosati, The role of graphene for electrochemical energy storage, Nat. Mater. 14 (3) (2015) 271–279.
[21] C.B. Zhu, R.E. Usiskin, Y. Yu, J. Maier, The nanoscale circuitry of battery electrodes, Science 358 (6369) (2017) 8.
[22] S.-H. Park, P.J. King, R. Tian, C.S. Boland, J. Coelho, C. Zhang, P. McBean, N. McEvoy, M.P. Kremer, D. Daly, J.N. Coleman, V. Nicolosi, High areal capacity battery electrodes enabled by segregated nanotube networks, Nat. Energy 4 (7) (2019) 560–567.
[23] L. Wen, F. Li, H.-M. Cheng, Carbon nanotubes and graphene for flexible electrochemical energy storage: from materials to devices, Adv. Mater. 28 (22) (2016) 4306–4337.
[24] W. Yuan, Y. Zhang, L. Cheng, H. Wu, L. Zheng, D. Zhao, The applications of carbon nanotubes and graphene in advanced rechargeable lithium batteries, J. Mater. Chem. 4 (23) (2016) 8932–8951.
[25] T. Hwang, J.K. Lee, J. Mun, W. Choi, Surface-modified carbon nanotube coating on high-voltage LiNi0.5Mn1.5O4 cathodes for lithium ion batteries, J. Power Sources 322 (2016) 40–48.
[26] H. Saneifar, N. Delaporte, K. Zaghib, D. Bélanger, Functionalization of the carbon additive of a high-voltage Li-ion cathode, J. Mater. Chem. 7 (4) (2019) 1585–1597.
[27] Z.Y. Ju, X. Zhang, S.T. King, C.D. Quilty, Y. Zhu, K.J. Takeuchi, E.S. Takeuchi, D.C. Bock, L. Wang, A.C. Marschilok, G.H. Yu, Unveiling the dimensionality effect of conductive fillers in thick battery electrodes for high-energy storage systems, Appl. Phys. Rev. 7 (4) (2020) 11.
[28] R. Xu, L.S. de Vasconcelos, J. Shi, J. Li, K. Zhao, Disintegration of meatball electrodes for LiNixMnyCozO2 cathode materials, Exp. Mech. 58 (4) (2018) 549–559.
[29] Z. Xu, M.M. Rahman, L. Mu, Y. Liu, F. Lin, Chemomechanical behaviors of layered cathode materials in alkali metal ion batteries, J. Mater. Chem. 6 (44) (2018) 21859–21884.
[30] Z. Huang, T. Xiong, X. Lin, M. Tian, W. Zeng, J. He, M. Shi, J. Li, G. Zhang, L. Mai, S. Mu, Carbon dioxide directly induced oxygen vacancy in the surface of lithium-rich layered oxides for high-energy lithium storage, J. Power Sources 432 (2019) 8–15.
[31] W. Zeng, F. Xia, W. Tian, F. Cao, J. Chen, J. Wu, R. Song, S. Mu, Single-crystal high-nickel layered cathodes for lithium-ion batteries: advantages, mechanism, challenges and approaches, Current Opinion Electrochemistry 31 (2022), 100831.
[32] K. Ishidzu, Y. Oka, T. Nakamura, Lattice volume change during charge/discharge reaction and cycle performance of Li[NixCoyMnz]O2, Solid State Ionics 288 (2016) 176–179.
[33] U.-H. Kim, E.-J. Lee, C.S. Yoon, S.-T. Myung, Y.-K. Sun, Compositionally graded cathode material with long-term cycling stability for electric vehicles application, Advanced Energy Materials 6 (22) (2016), 1601417.
[34] A.O. Kondrakov, A. Schmidt, J. Xu, H. Geßwein, R. Mönig, P. Hartmann, H. Sommer, T. Brezesinski, J. Janek, Anisotropic lattice strain and mechanical degradation of high- and low-nickel NCM cathode materials for Li-ion batteries, J. Phys. Chem. C 121 (6) (2017) 3286–3294.
[35] H.H. Ryu, K.J. Park, C.S. Yoon, Y.K. Sun, Capacity fading of Ni-rich Li NixCoyMn1-x-y O-2 (0.6 <= x <= 0.95) cathodes for high-energy-density lithium-ion batteries: bulk or surface degradation? Chem. Mater. 30 (3) (2018) 1155–1163.
[36] S.H. Xia, L.Q. Mu, Z.R. Xu, J.Y. Wang, C.X. Wei, L. Liu, P. Pianetta, K.J. Zhao, X.Q. Yu, F. Lin, Y.J. Liu, Chemomechanical interplay of layered cathode materials undergoing fast charging in lithium batteries, Nanomater. Energy 53 (2018) 753–762.
[37] C.D. Quilty, D.C. Bock, S. Yan, K.J. Takeuchi, E.S. Takeuchi, A.C. Marschilok, Probing sources of capacity fade in LiNi0.6Mn0.2Co0.2O2 (NMC622): an operando XRD study of Li/NMC622 batteries during extended cycling, J. Phys. Chem. C 124 (15) (2020) 8119–8128.
[38] S. Muller, P. Pietsch, B. Brandt, P. Baade, V. De Andrade, F. De Carlo, V. Wood, Quantification and modeling of mechanical degradation in lithium-ion batteries based on nanoscale imaging, Nat. Commun. 9 (2018) 8.
[39] R. Xu, Y. Yang, F. Yin, P.F. Liu, P. Cloetens, Y.J. Liu, F. Lin, K.J. Zhao, Heterogeneous damage in Li-ion batteries: experimental analysis and theoretical modeling, J. Mech. Phys. Solid. 129 (2019) 160–183.
[40] Y. Yang, R. Xu, K. Zhang, S.J. Lee, L.Q. Mu, P.F. Liu, C.K. Waters, S. Spence, Z.R. Xu, C.X. Wei, D.J. Kautz, Q.X. Yuan, Y.H. Dong, Y.S. Yu, X.H. Xiao, H.K. Lee, P. Pianetta, P. Cloetens, J.S. Lee, K.J. Zhao, F. Lin, Y.J. Liu, Quantification of heterogeneous degradation in Li-ion batteries, Advanced Energy Materials 9 (25) (2019) 11.
[41] X. Liu, A. Ronne, L.-C. Yu, Y. Liu, M. Ge, C.-H. Lin, B. Layne, P. Halstenberg, D.S. Maltsev, A.S. Ivanov, S. Antonelli, S. Dai, W.-K. Lee, S.M. Mahurin, A.I. Frenkel, J.F. Wishart, X. Xiao, Y.-c.K. Chen-Wiegart, Formation of three-dimensional bicontinuous structures via molten salt dealloying studied in real-time by in situ synchrotron X-ray nano-tomography, Nat. Commun. 12 (1) (2021) 3441.
[42] M.Y. Ge, D.S. Coburn, E. Nazaretski, W.H. Xu, K. Gofron, H.J. Xu, Z.J. Yin, W.K. Lee, One-minute nano-tomography using hard X-ray full-field transmission microscope, Appl. Phys. Lett. 113 (8) (2018), 083109.
[43] R. Vescovi, M. Du, V. de Andrade, W. Scullin, D. Gursoy, C. Jacobsen, Tomosaic: efficient acquisition and reconstruction of teravoxel tomography data using limited-size synchrotron X-ray beams, J. Synchrotron Radiat. 25 (2018) 1478–1489.
[44] J. Nelson Weker, M.F. Toney, Emerging in situ and operando nanoscale X-ray imaging techniques for energy storage materials, Adv. Funct. Mater. 25 (11) (2015) 1622–1637.
[45] P. Pietsch, V. Wood, X-ray tomography for lithium ion battery research: a practical guide, Annu. Rev. Mater. Res. 47 (1) (2017) 451–479.
[46] C.H. Zhao, T. Wada, V. De Andrade, D. Gursoy, H. Kato, Y.C.K. Chen-Wiegart, Imaging of 3D morphological evolution of nanoporous silicon anode in lithium ion battery by X-ray nano-tomography, Nanomater. Energy 52 (2018) 381–390.
[47] J.J. Wang, Y.C.K. Chen-Wiegart, C. Eng, Q. Shen, J. Wang, Visualization of anisotropic-isotropic phase transformation dynamics in battery electrode particles, Nat. Commun. 7 (2016).
[48] C.-H. Lin, K. Sun, M. Ge, L.M. Housel, A.H. McCarthy, M.N. Vila, C. Zhao, X. Xiao, W.-K. Lee, K.J. Takeuchi, E.S. Takeuchi, A.C. Marschilok, Y.-c.K. Chen-Wiegart, Systems-level investigation of aqueous batteries for understanding the benefit of water-in-salt electrolyte by synchrotron nanoimaging, Science Advances 6 (10) (2020), eaay7129.
[49] J. Lim, Y. Li, D.H. Alsem, H. So, S.C. Lee, P. Bai, D.A. Cogswell, X. Liu, N. Jin, Y.-s. Yu, N.J. Salmon, D.A. Shapiro, M.Z. Bazant, T. Tyliszczak, W.C. Chueh, Origin and hysteresis of lithium compositional spatiodynamics within battery primary particles, Science 353 (6299) (2016) 566–571.
[50] C.-H. Lin, L. Wang, S.T. King, J. Bai, L.M. Housel, A.H. McCarthy, M.N. Vila, H. Zhu, C. Zhao, L. Zou, S. Ghose, X. Xiao, W.-K. Lee, K.J. Takeuchi, A.C. Marschilok, E.S. Takeuchi, M. Ge, Y.-c.K. Chen-Wiegart, Probing kinetics of water-in-salt aqueous batteries with thick porous electrodes, ACS Cent. Sci. 7 (10) (2021) 1676–1687.
[51] G. Qian, H. Huang, F. Hou, W. Wang, Y. Wang, J. Lin, S.-J. Lee, H. Yan, Y.S. Chu, P. Pianetta, X. Huang, Z.-F. Ma, L. Li, Y. Liu, Selective dopant segregation modulates mesoscale reaction kinetics in layered transition metal oxide, Nanomater. Energy 84 (2021), 105926.
[52] S. Yu, Application of Parzen window in filter back projection algorithm, IOP Conf. Ser. Mater. Sci. Eng. 392 (6) (2018), 062183.
[53] D.M. Pelt, D. Gursoy, W.J. Palenstijn, J. Sijbers, F. De Carlo, K.J. Batenburg, Integration of TomoPy and the ASTRA toolbox for advanced processing and reconstruction of tomographic synchrotron data, J. Synchrotron Radiat. 23 (2016) 842–849.
[54] F. Meyer, Topographic distance and watershed lines, Signal Process. 38 (1) (1994) 113–125.
[55] P. Soille, Morphological Image Analysis : Principles and Applications, second ed., Springer, Berlin, 2003.
[56] M. Ebner, F. Geldmacher, F. Marone, M. Stampanoni, V. Wood, X-ray tomography of porous, transition metal oxide based lithium ion battery electrodes, Advanced Energy Materials 3 (7) (2013) 845–850.
[57] C.R. Maurer, R.S. Qi, V. Raghavan, A linear time algorithm for computing exact Euclidean distance transforms of binary images in arbitrary dimensions, IEEE Trans. Pattern Anal. Mach. Intell. 25 (2) (2003) 265–270.
[58] A.R. Rao, B.G. Schunck, Computing oriented texture fields, CVGIP Graph. Models Image Process. 53 (2) (1991) 157–185.
[59] J. Weickert, Coherence-enhancing diffusion filtering, Int. J. Comput. Vis. 31 (2–3) (1999) 111–127.
[60] J. Canny, A computational approach to edge-detection, IEEE Trans. Pattern Anal. Mach. Intell. 8 (6) (1986) 679–698.
[61] S. van der Walt, J.L. Schonberger, J. Nunez-Iglesias, F. Boulogne, J.D. Warner, N. Yager, E. Gouillart, T. Yu, C. Scikit, Image, scikit-image: image processing in Python, PeerJ 2 (2014) 18.
[62] V.A. Dahl, N. Jeppesen, Structure Tensor 2D and 3D Implementation for Python, 2020.
[63] R. Hovden, M.D. Hanwell, U. Ayachit, Y. Jiang, R. Maynard, D.A. Muller, Repeatable and transferable processing for electron tomography: an open platform for visualization and reconstruction of 3D materials, Microsc. Microanal. 21 (S3) (2015) 2407–2408.
[64] Dragonfly 2020.2 [Computer Software], Object Research Systems (ORS) Inc,

Montreal, Canada, 2020 software available at: http://www.theobjects.com/dragonfly.
[65] M.Y. Ge, W.K. Lee, PyXAS - an open-source package for 2D X-ray near-edge spectroscopy analysis, J. Synchrotron Radiat. 27 (2020) 567–575.
[66] B. Ravel, M. Newville, ATHENA, artemis, hephaestus: data analysis for X-ray absorption spectroscopy using IFEFFIT, J. Synchrotron Radiat. 12 (2005) 537–541.
[67] R. Xu, L.S. de Vasconcelos, J. Shi, J. Li, K. Zhao, Disintegration of meatball electrodes for LiNi (x) Mn (y) Co (z) O-2 cathode materials, Exp. Mech. 58 (4) (2018) 549–559.
[68] Y.W. Mao, X.L. Wang, S.H. Xia, K. Zhang, C.X. Wei, S. Bak, Z. Shadike, X.J. Liu, Y. Yang, R. Xu, P. Pianetta, S. Ermon, E. Stavitski, K.J. Zhao, Z.R. Xu, F. Lin, X.Q. Yang, E.Y. Hu, Y.J. Liu, High-voltage charging-induced strain, heterogeneity, and micro-cracks in secondary particles of a nickel-rich layered cathode material, Adv. Funct. Mater. 29 (18) (2019) 11.
[69] Z.S. Jiang, J.Z. Li, Y. Yang, L.Q. Mu, C.X. Wei, X.Q. Yu, P. Pianetta, K.J. Zhao, P. Cloetens, F. Lin, Y.J. Liu, Machine-learning-revealed statistics of the particle-carbon/binder detachment in lithium-ion battery cathodes, Nat. Commun. 11 (1) (2020) 9.
[70] E. Ligneel, B. Lestriez, A. Hudhomme, D. Guyomard, Effects of the solvent concentration (solid loading) on the processing and Properties of the composite electrode, J. Electrochem. Soc. 154 (3) (2007) A235.
[71] W. Porcher, B. Lestriez, S. Jouanneau, D. Guyomard, Design of aqueous processed thick LiFePO[sub 4] composite electrodes for high-energy lithium battery, J. Electrochem. Soc. 156 (3) (2009) A133.
[72] C.-C. Li, Y.-W. Wang, Binder distributions in water-based and organic-based LiCoO2 electrode sheets and their effects on cell performance, J. Electrochem. Soc. 158 (12) (2011) A1361.
[73] A. Etiemble, N. Besnard, A. Bonnin, J. Adrien, T. Douillard, P. Tran-Van, L. Gautier, J.C. Badot, E. Maire, B. Lestriez, Multiscale morphological characterization of process induced heterogeneities in blended positive electrodes for lithium–ion batteries, J. Mater. Sci. 52 (7) (2017) 3576–3596.
[74] J. Li, C. Daniel, S.J. An, D. Wood, Evaluation residual moisture in lithium-ion battery electrodes and its effect on electrode performance, MRS Advances 1 (15) (2016) 1029–1035.
[75] B.J. Hwang, Y.W. Tsai, D. Carlier, G. Ceder, A combined computational/experimental study on LiNi1/3Co1/3Mn1/3O2, Chem. Mater. 15 (19) (2003) 3676–3682.
[76] W.S. Yoon, M. Balasubramanian, K.Y. Chung, X.Q. Yang, J. McBreen, C.P. Grey, D.A. Fischer, Investigation of the charge compensation mechanism on the electrochemically Li-ion deintercalated Li1-xCo1/3Ni1/3Mn1/3O2 electrode system by combination of soft and hard x-ray absorption spectroscopy, J. Am. Chem. Soc. 127 (49) (2005) 17479–17487.
[77] N. Besnard, A. Etiemble, T. Douillard, O. Dubrunfaut, P. Tran-Van, L. Gautier, S. Franger, J.-C. Badot, E. Maire, B. Lestriez, Multiscale morphological and electrical characterization of charge transport limitations to the power performance of positive electrode blends for lithium-ion batteries, Advanced Energy Materials 7 (8) (2017), 1602239.